Fatigue Criticality Assessment of Volumetric Defects in Notched Specimens: A Non-destructive Approach

Arun Poudel[a,b], Jonathan Pegues[a,b], Matthew Kelly[c], Shuai Shao[a,b], Nima Shamsaei[a,b,*]

[a] National Center for Additive Manufacturing Excellence (NCAME), Auburn University, Auburn, AL, 36849, USA

[b] Department of Mechanical Engineering, Auburn University, Auburn, AL, 36849, USA

[c] U.S. Army DEVCOM Ground Vehicles System Center (GVSC), Warren, MI 48092 USA

* Corresponding author: shamsaei@auburn.edu

Phone: (334) 844-4839

To be submitted to:

Fatigue & Fracture of Engineering Materials & Structures

May 2025

Abstract

This study utilizes linear elastic fracture mechanics to assess fatigue criticality of volumetric defects in notched specimens with varying geometries. Contrasting to the existing literature, this study assesses the fatigue criticality of defects, prior to fracture, via a non-destructive inspection technique, i.e., X-ray computed tomography (XCT). Treating volumetric defects as cracks, based on Murakami's definition, the approach calculates their Mode-I stress intensity factor (SIF) with their local stresses obtained via linear elastic finite element analysis, and utilizes the SIF to represent their criticality. For validation, cylindrical and flat specimens with notch root radii of 5 mm and 50 mm of AlSi10Mg and 17-4 precipitation hardened stainless steel were fabricated, XCT scanned, and tested under fatigue loading. All crack initiating defects, observed from fractography, fell within the 99.3 percentile of the defects with the highest stress intensity factor in the respective specimens.

Keywords:

Additive manufacturing; Defect criticality; Non-destructive inspection/testing/evaluation (NDI/NDT/NDE); X-ray computed tomography (XCT); Fatigue

Nomenclature

e	Centroidal distance between two neighboring defects
$\sqrt{area}$	Square root of projected area of a defect on the loading plane
δ-Fe	Delta-ferrite
$K_{I(Max.)}$	Maximum mode-I stress intensity factor during a loading cycle
$K_{t(local)}$	Local elastic stress concentration factor
ρ	Notch root radius
R	Recommended condition
$\sigma_{Max.}$	Maximum applied nominal stress
U	Underheated condition
Y	Murakami's location-dependent factor

1 Introduction

Additive manufacturing (AM) processes, such as laser powder bed fusion (L-PBF), are prone to induce volumetric defects in parts, which act as stress concentrators and often are fatigue-critical in surface machined condition [1–4]. Variation in the defects' geometrical features resulting from slight perturbations in processing conditions can lead to significant scatter in fatigue lives, often well beyond two orders of magnitude in the high cycle fatigue regime [5–7]. This suggests that defect content, thus the material properties, can significantly vary from coupons to parts and from one part to another [8–10]. The uncertainties associated with such variations can not only make quantifying defects' critical effects on part's fatigue behavior difficult but also render the conventional, process-lockdown based qualification approaches impractical [11,12]. These challenges are further exacerbated by AM's ability to fabricate geometrically complex parts, which often comprise an abundance of notch-like features [13–16]. The stress concentration of these features interacts with that of the volumetric defects to potentially accelerate fatigue crack initiation [15,17–20]. Since such an acceleration only affects the defects present in the vicinity of notches, the uncertainty in the fatigue performance of AM parts can be further increased.

The uncertainty of defect content in critical locations of AM parts can be ascertained, at least partially, by the application of an effective non-destructive inspection (NDI) technique, such as X-ray computed tomography (XCT) [21–25]. For instance, modern high-resolution XCT systems can reliably reveal the geometry, size, and spatial distributions of volumetric defects larger than 20 μm in a reasonably sized notch specimen (i.e., a diameter of 5 mm) made of relatively dense material (i.e., 17-4 PH stainless steel (SS)) [22,26,27]. Nevertheless, due to the complex interplay between the stress fields of notches and volumetric defects, quantifying the critical effects of volumetric defects in the presence of notches remains elusive. Specifically, due to the presence of a decaying stress field away from the notch roots, the existing approaches for notch free members [5,28–31] that categorize defects into internal/surface ones and calculate their stress intensity factors in each category assuming a uniform stress may not be directly applicable.

This study utilizes linear elastic fracture mechanics (LEFM) to assess the fatigue criticality of volumetric defects detected via an NDI technique, i.e., XCT, for the qualification of AM parts.

The existing literature utilizes the LEFM approach, such as Murakami's $\sqrt{area}$ approach, to measure the post-fracture critical defect's size and its equivalent SIF [32,33]. Contrasting to the literature, this work assesses the fatigue criticality of defects using a non-destructive technique, enabling the identification of potentially critical defects prior to destructive analysis. Furthermore, this study performed such fatigue criticality assessments for complex AM parts; these parts have different geometry notches in them. In this study, the NDI-based approach relies on XCT to quantify the content of volumetric defects in a part, and finite element method performed on part's computer aided design (CAD) model to analyze the local stress environment of each defect. By treating each defect as a crack equivalent, a defect's criticality is represented by its Mode-I stress intensity factor (SIF) calculated via Murakami's approach, accounting for the local stress. This approach is then validated on two types of notched fatigue specimens (cylindrical and flat) with two notch root radii (5 mm and 50 mm) made of both AlSi10Mg and 17-4 PH SS. For validation, the critical crack initiating defect was identified using fractography for each specimen, matched with the one detected from XCT, and its corresponding SIF, calculated using the NDI-based approach, was compared with the others in the same specimen.

2 Method and materials

2.1 Methodology of the NDI-based approach

The procedure to quantify the fatigue criticality of volumetric defects in notched specimens is illustrated in **Fig. 1**. First, the notched specimens were scanned using an XCT technique to extract the volumetric defects' information such as their sizes and locations. To extract defect information, the tomography data was processed to obtain greyscale images, followed by gradient and binary operations, to isolate the defect boundary from the surrounding matrix, as shown in **Fig. 2**(a-c). The boundary filled binarized defect morphology, shown in **Fig. 2**(d), was processed using MATLAB to extract the necessary defect information. It should be noted that this approach slightly overestimates the sizes of the detected volumetric defects. Second, the local stresses at different locations within the notched specimens were quantified using linear elastic finite element analysis (LEFEA).

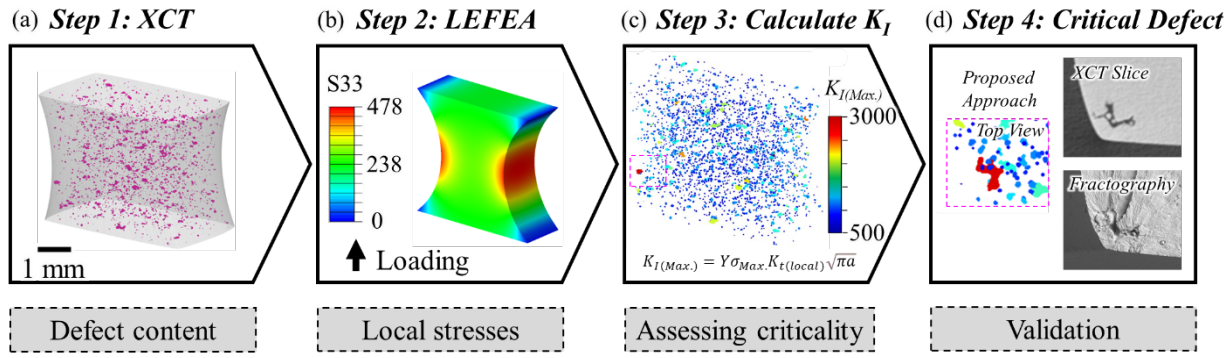

Fig. 1 Diagram showing different steps to quantify the fatigue criticality of volumetric defects in notched specimens: (a) Defect content quantified via XCT, (b) local stresses analyzed via LEFEA, (c) SIF calculated using LEFM, and (d) validation performed using fractography.

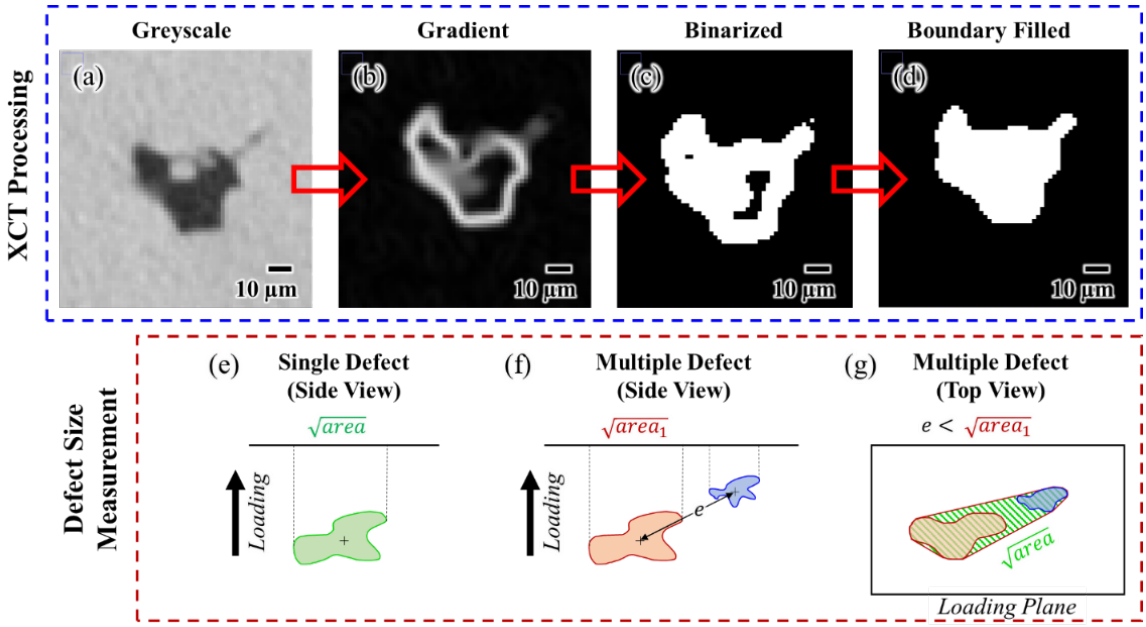

Fig. 2 Different stages of XCT data post-processing: (a) greyscale, (b) gradient, (c) binarized, and (d) boundary filled. Schematic illustration of defect size measurement in the case of (e) single and (f, g) multiple (two) nearby defects.

LEFEA was performed using ABAQUS® software for ρ *5 mm* and ρ *50 mm* cylindrical and flat specimens. It is worth mentioning that the finite element (FE) models and the specimens used for validation had similar geometries. For cylindrical specimens, two-dimensional axisymmetric FE models were created (see **Fig. 3**(a)). For flat specimens, one-eighth of the full models were created, assuming symmetric boundary conditions in all three planes, i.e., X_1-X_2, X_1-X_3, and X_2-X_3, as shown in **Fig. 3**(d). The FE models for cylindrical specimens were meshed using

CAX6M, 6-node modified quadratic axisymmetric triangle elements, while C3D10, 10-node quadratic tetrahedron elements—offering good geometric conformity to notches, were used for flat specimens. For each model, a mesh convergence study was performed, resulting in the smallest element size of ~0.5 μm at the notch root. The converged meshes for each of the FE models are presented in **Figs. 3**(c-f). A remote displacement of 100 μm was applied, as indicated using black arrows in **Figs. 3**(c-f). The resulting normal stresses, along the loading direction, σ_{33}, were extracted from seven different heights relative to the notch root plane, i.e., h_{center}/h_0, where h_{center} is the distance of the crack initiation site from the notch root plane and h_0 is the total height of the notch geometry, schematically shown in **Fig. 3**(g). For flat specimens, normal stresses from both center and lateral planes (schematically shown in **Fig. 3**(h)) were extracted. The extracted normal stresses, σ_{33}, were normalized using the nominal stress, σ_0, at the notch root plane to obtain the local stress concentration factor, i.e., $K_{t(local)} = \sigma_{33}/\sigma_0$.

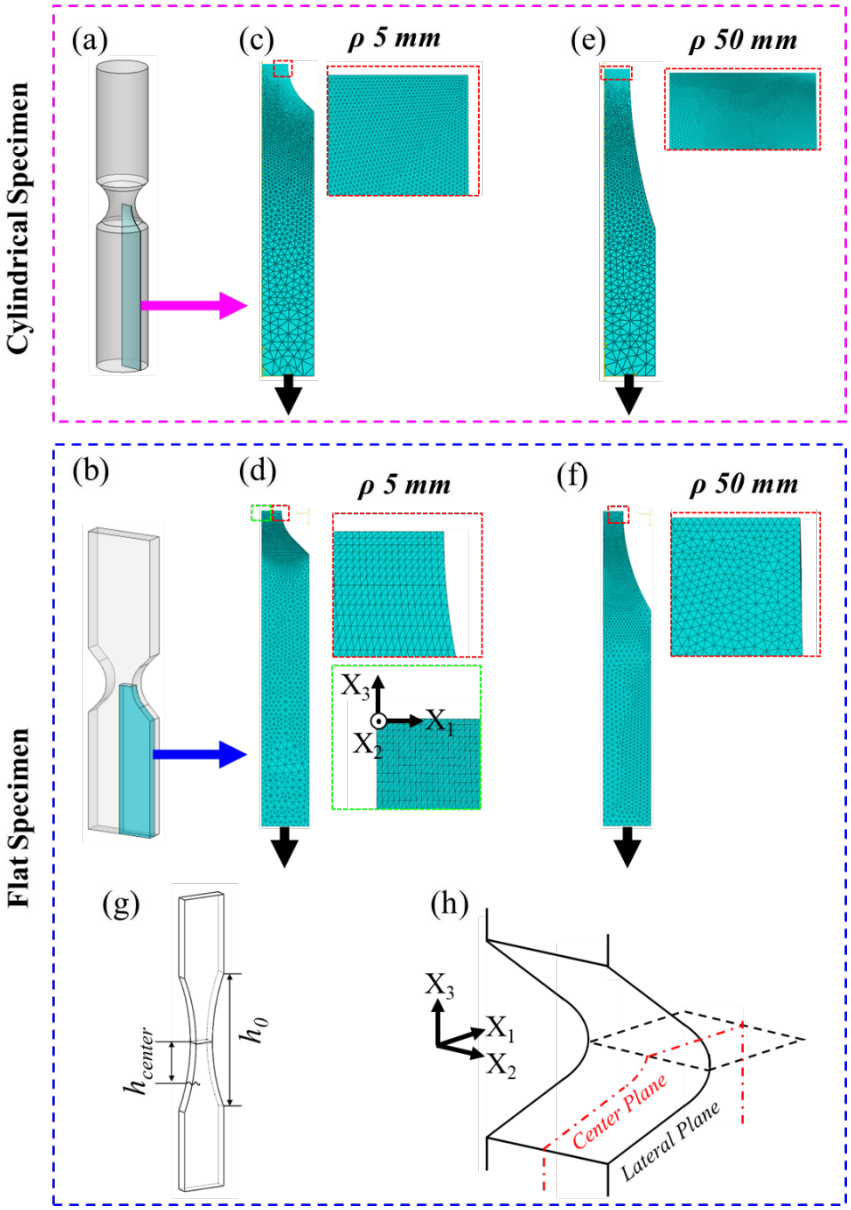

Fig. 3 (a, b) Geometries and FE meshes for (c, d) *ρ 5 mm* and (e, f) *ρ 50 mm* cylindrical and flat notched specimens. Schematics showing (g) relative height of crack initiation (h_{center}/h_0), and (h) center and lateral planes in the flat specimen.

Third, Mode-I SIF for every volumetric defect within the XCT scan volume was calculated using LEFM, i.e., Murakami's approach. Assuming a defect-crack equivalency, the Mode-I SIF for a volumetric defect under the intended cyclic loading was calculated using:

$$K_{I(Max.)} = Y\sigma_{Max.}K_{t(local)}\sqrt{\pi\sqrt{area}}\,, \tag{1}$$

where $K_{I(Max.)}$ is the maximum Mode-I SIF during a loading cycle, Y is Murakami's location-dependent factor (0.5 for internal and 0.65 for surface defects [34]), $\sigma_{Max.}$ is the maximum applied nominal stress, $K_{t(local)}$ is the local stress concentration factor at the defect's centroidal location [35,36], and $\sqrt{area}$ is the defect size. The calculated SIF represented the criticality of notch geometry, defect's size and location, on the fatigue behavior. During XCT processing, the defect's size was measured in accordance with Murakami's approach, i.e., the square root of the area of a convex hull around the projected shape of the defect onto the loading plane [37]. Additionally, the combined influence of a cluster of defects on the fatigue behavior was accounted for by calculating the $\sqrt{area}$ of the convex hull surrounding the cluster, again based on Murakami's approach. For any defect, if the centroidal distance to its smaller neighbor is less than its own size, then the neighbor is included in the cluster with the defect as schematically shown in **Figs. 2**(f & g). Note that, for a cluster, the calculated SIF was assigned to all of its defects. The obtained SIF was used to represent the fatigue criticality of volumetric defects in notched specimens (see **Fig. 1**(c)), i.e., defects with higher SIF were assumed to possess higher probability to initiate fatigue cracks. Such a LEFM-based approach to assess the fatigue criticality of defects is applicable under small loads where the elasticity governs deformation. In the presence of notch root plasticity, the criticality of volumetric defects attenuates due to the blunting effect, making the difference in the criticality among defects smaller. Nevertheless, the rankings provided by the LEFM-based approach are still expected to be valid. Finally, validation of the approach was performed by comparing the top ranked defects having the highest SIF with the ones observed via fractography (see **Fig. 1**(d)).

2.2 Materials and specimen geometries

The procedure illustrated in **Fig. 1** was applied to the notched fatigue specimens fabricated and tested for some earlier works [35,36], which included both flat and cylindrical ones with different notch root radii and were made from both AlSi10Mg and 17-4 PH SS. The cylindrical and flat specimens (whose geometries are shown in **Fig. 4**) were machined, respectively, from bars and rectangular blocks fabricated from two different L-PBF machines, and their axial directions were aligned with the build directions. AlSi10Mg was fabricated using Renishaw RenAM 500Q Flex, and 17-4 PH SS using 3D SYSTEMS DMP Flex 350B. To vary the defect content within

notched specimens, both the manufacturer recommended process parameters (referred to as the R specimens) and the modified ones to induce underheated condition (referred to as the U specimens) were used for fabrication.

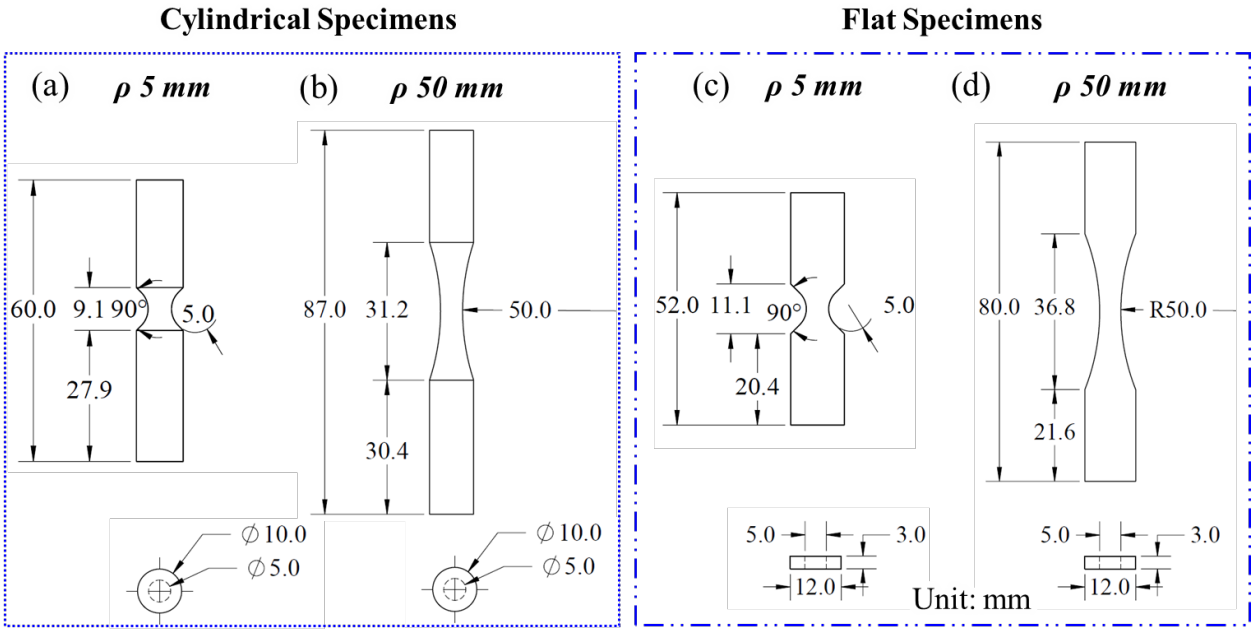

Fig. 4 Geometries and dimensions of (a, b) cylindrical and (c, d) flat notched specimens with notch root radii of 5 mm and 50 mm.

Prior to machining, AlSi10Mg parts were stress-relieved (SR) at 285 °C for 2 hours in accordance with AMS 2771 standard [38], while 17-4 PH SS parts were SR at 700 °C for an hour, followed by CA-H1025, in accordance with ASTM A693 standard [39]. For convenience, specimens with notch root radii of 5 mm and 50 mm will be referred to as *ρ 5 mm* and *ρ 50 mm* in the remaining sections of this article. After machining, the specimens were ground and polished using sandpapers with grits ranging from P240 to P1200. These specimens were scanned using an XCT technique on a ZEISS Xradia 620 Versa machine with a voxel size of 6.5 µm. To avoid false detection from noise, any defects/features smaller than 20 µm were not considered for analysis.

The notched specimens were subjected to force-controlled fatigue tests and after failure, fractography was performed to identify the crack initiating defect. AlSi10Mg specimens were subjected to maximum nominal stresses ranging from 100 to 150 MPa, and 17-4 PH SS from 800 to 1200 MPa at a stress ratio of 0.1. Considering sixteen different configurations, i.e., 2 materials

× 2 fabrication conditions × 4 notch geometries, 32 specimens (2 per configuration) were analyzed and tested. Out of 32 specimens, 15 specimens showed fatigue crack initiation from volumetric defects within the scan volume. The remaining specimens either showed crack initiation from microstructural features, defects outside the scan volume, or reached run-out during fatigue testing.

3 Results and discussion

3.1 Local stress concentrations in cylindrical and flat notched specimens

The local stress concentration factors, $K_{t(local)}$, for ρ *5 mm* and ρ *50 mm* cylindrical and flat notched specimens, obtained via LEFEA, are plotted against the normalized distance ahead of the notch surface, i.e., l/l_0, where l is the distance ahead of the notch surface and l_0 is the distance from the notch surface to the symmetric axis, in **Fig. 5**. For both cylindrical and flat specimens, ρ *5 mm* showed higher stress concentration factor compared to ρ *50 mm*, at the notch root. Ahead of the notch root, $K_{t(local)}$ for ρ *5 mm* decreased at a higher rate compared to ρ *50 mm* (see **Fig. 5**), indicating a higher rate of stress field decay in sharper notches. Due to the variation in the notch stress field, the $K_{t(local)}$ trends ahead of the notch surface shifted from a decreasing trend, near the notch root plane, to an increasing trend at higher relative heights (h_{center}/h_0), especially for ρ *5 mm* specimens. For flat specimens, ρ *5 mm* showed slightly lower $K_{t(local)}$ at the lateral plane compared to the center plane, likely due to the influence of plane stress condition in the lateral free surfaces. For ρ *50 mm*, $K_{t(local)}$ in both center and lateral planes were near identical (see **Fig. 5**(c)). The $K_{t(local)}$, presented in **Figs. 5**(a-c), was utilized to calculate the SIF of volumetric defects at different locations within the notched specimens, using Eq. 1. Details on approximation functions utilized to calculate the $K_{t(local)}$ for cylindrical and flat notched specimens are provided in **Supplemental Materials Section S1**.

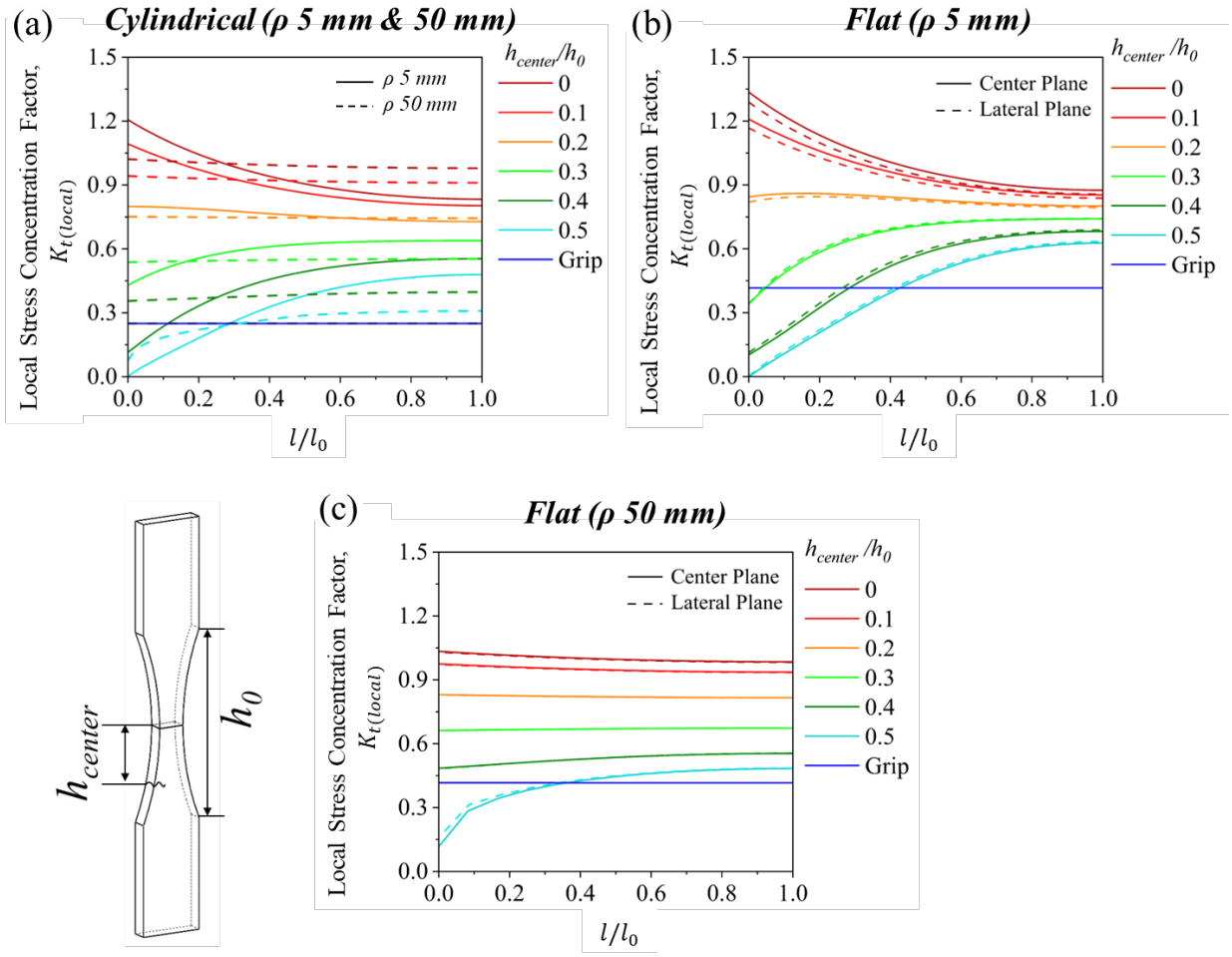

Fig. 5 Local stress concentration factors at different heights relative to the notch root plane and distances away from the notch surface, for *ρ 5 mm* and *ρ 50 mm* (a) cylindrical and (b, c) flat notched specimens.

3.2 Effectiveness of the NDI-based approach

Based on the SIF calculated according to the procedure outlined in **Fig. 1**, the fatigue criticality of volumetric defects within AlSi10Mg and 17-4 PH SS notched specimens could be quantitatively represented. To be exact, the SIF should signify the tendency of a volumetric defect to initiate a fatigue crack, e.g., the defect with the highest SIF in a specimen should be responsible for the initiation of the fatigue failure. Realizing this, the efficacy of the utilized NDI-based approach can be validated by comparing top ranked defects from the XCT analysis with the fatigue critical defects identified from fractography after fatigue tests. The critical defects within the XCT

scan volume were identified by utilizing their location information (both in and out of the fracture plane) obtained from the fractured specimens.

Fig. 6 demonstrates the efficacy of the NDI-based approach using ρ *5 mm* and ρ *50 mm* AlSi10Mg cylindrical notched specimens that were subjected to 125 MPa and 150 MPa maximum nominal stresses as examples. Implementing the procedure outlined in **Fig. 1**, SIF for all volumetric defects within the scan volumes were calculated and visualized in **Figs. 6**(a & b). Furthermore, the defects with the highest SIF were identified (pointed using arrows in greyscale images in **Figs. 6**(c & d)) and compared to the critical defects in the fracture surface of the respective specimens, **Figs. 6**(e & f). Volumetric defects with the highest SIF were found to initiate critical fatigue cracks in both ρ *5 mm* and ρ *50 mm* AlSi10Mg specimens. Interestingly, the two crack initiating defects in both ρ *5 mm* and ρ *50 mm* (see **Figs. 6**(e & f)) had the highest and the second highest SIF among all defects within the specimen.

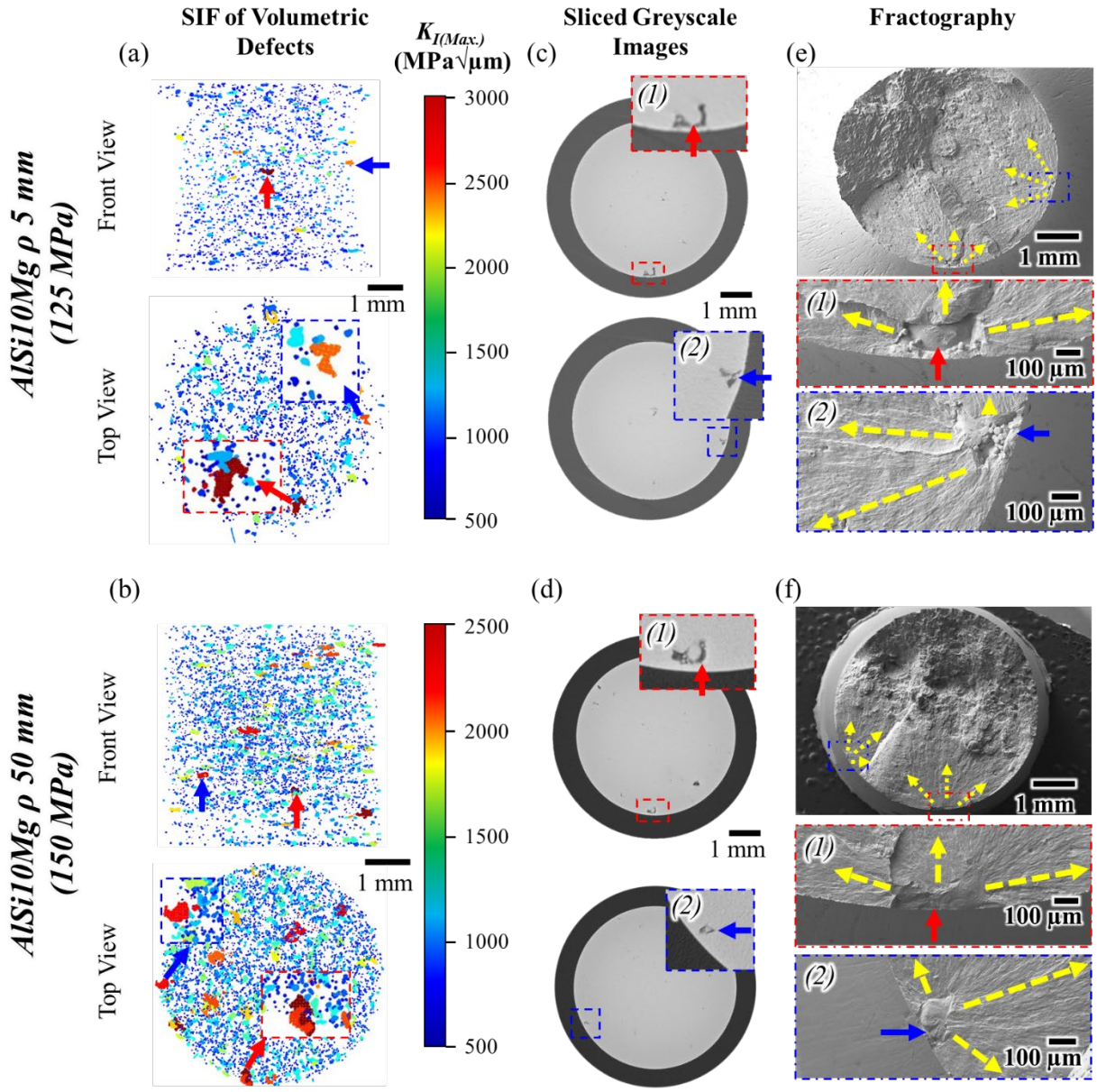

Fig. 6 (a, b) Visualization of volumetric defects, colored according to their SIF, within the XCT scan volume, (c, d) sliced greyscale images showing the critical defects, and (e, f) fractography images showing the fatigue crack initiation sites in *ρ 5 mm* and *ρ 50 mm* AlSi10Mg cylindrical specimens.

Similarly, **Fig. 7** shows additional examples demonstrating the efficacy of the NDI-based approach using *ρ 5 mm* and *ρ 50 mm* AlSi10Mg flat notched specimens subjected to 150 MPa and 125 MPa maximum nominal stresses. As a note, the raw XCT data for notched specimens shown

in **Figs. 6** and **7** are provided in the **Supplemental Materials Section S2**. Fractography images show the presence of critical defects at the corner and the faces of notches for *ρ 5 mm* and *ρ 50 mm* specimens, respectively (see **Figs. 7**(e & f)). The critical defect that initiated the crack and caused fatigue failure had the highest SIF among all defects for both *ρ 5 mm* and *ρ 50 mm* flat notched specimens. In addition to what's shown in **Fig. 7**, fatigue cracks were also found, in other specimens, to initiate from lateral surfaces, i.e., the flat side surfaces. Given the lesser degree of stress concentration, the crack initiating defects from lateral surfaces were typically larger. Regardless, the approach was robust enough to address the complex stress environment imposed by the flat notched specimens. Similar confirmation on the efficacy of the NDI-based approach using cylindrical and flat 17-4 PH SS notched specimens was obtained, as shown in **Fig. 8**.

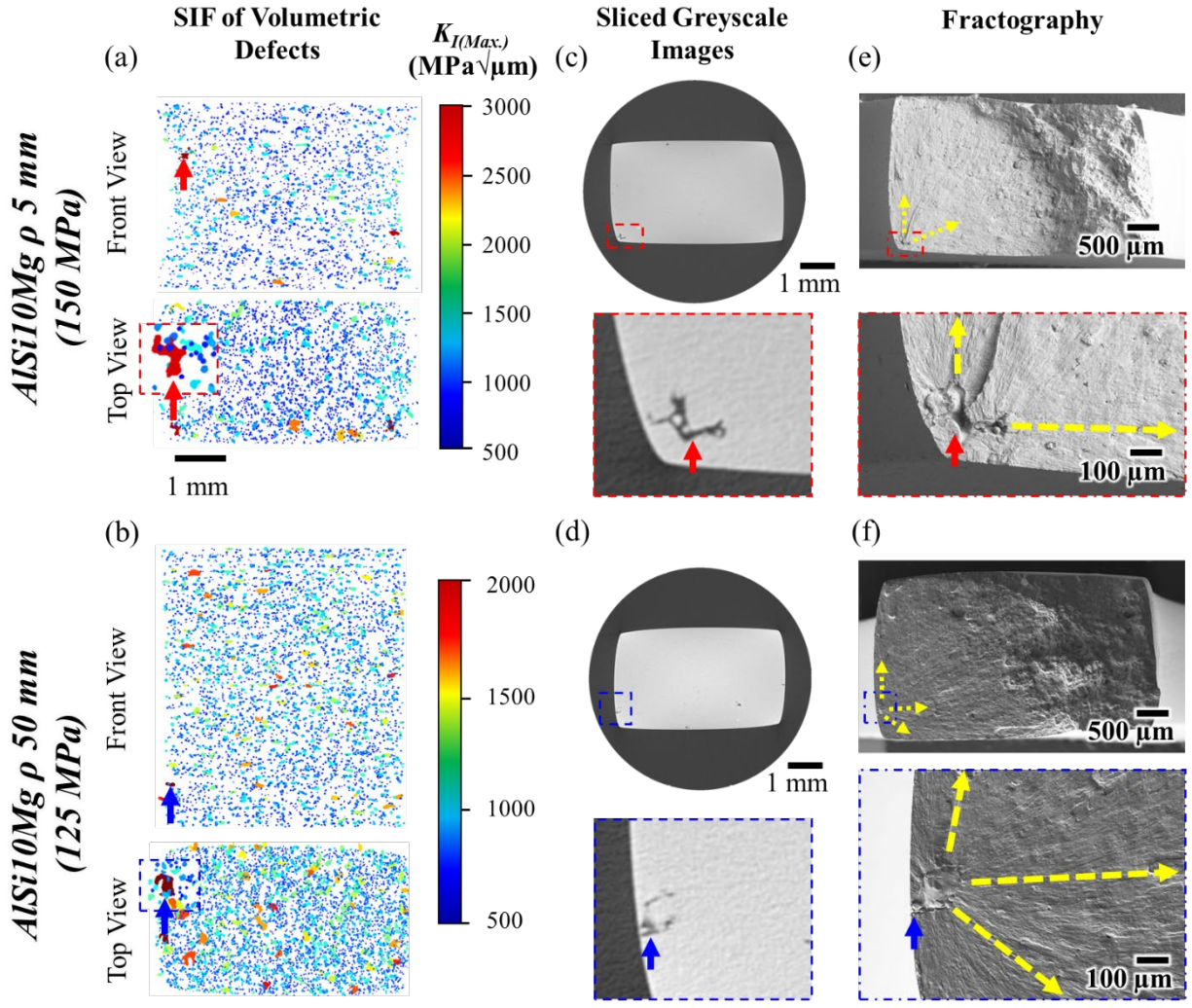

Fig. 7 (a, b) Visualization of volumetric defects, colored according to their SIF, within the XCT scan volume, (c, d) sliced greyscale images showing the critical defects, and (e, f) fractography images showing the fatigue crack initiation sites in *ρ 5 mm* and *ρ 50 mm* AlSi10Mg flat notched specimens.

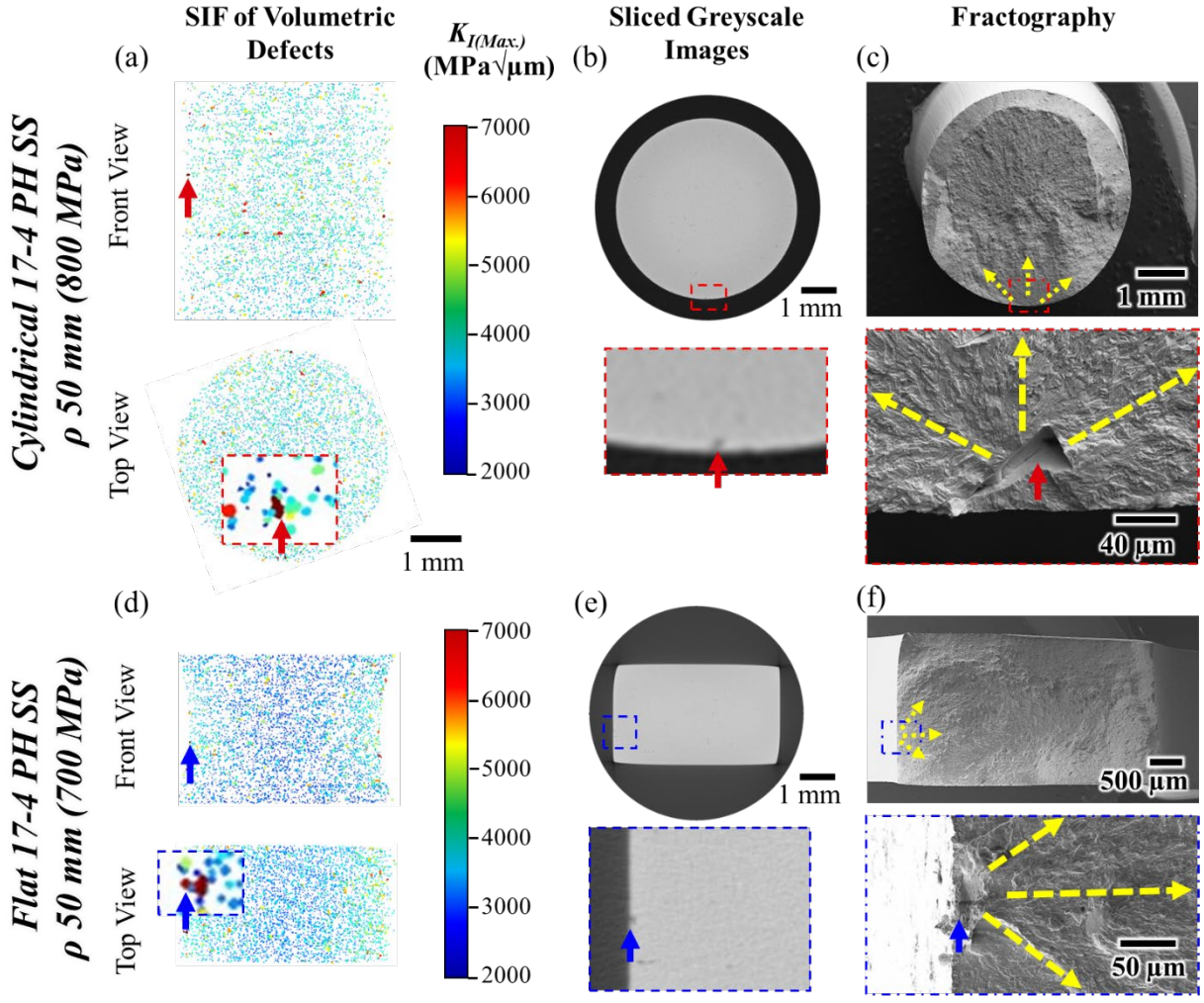

Fig. 8 (a, b) Visualization of volumetric defects, colored according to their SIF, within the XCT scan volume, (c, d) sliced greyscale images showing the critical defects, and (e, f) fractography images showing the fatigue crack initiation sites in cylindrical *ρ 50 mm* and flat *ρ 5 mm* 17-4 PH SS specimens.

Overall, the NDI-based approach performed well in assessing the fatigue criticality of volumetric defects in notched specimens. **Table 1** lists the information of all 17 fatigue critical defects observed in this study (i.e., from the 15 specimens that experienced fatigue crack initiation from volumetric defects) including their size measured via both XCT and fractography, normalized

SIF (calculated with size measured via XCT), and the corresponding rankings in SIF among other defects in the same specimens. For completeness, the details of the specimens including the material, the geometry type, and the notch root radius are also provided. It is worth mentioning that the critical defect size obtained via fractography was measured in accordance with Murakami's $\sqrt{area}$ approach. All crack initiating defects were found to be within the 99.3 percentile of the defects with the highest stress intensity factor in the respective notched specimens. Additionally, the NDI-based approach showed critical defects in ten specimens out of fifteen to have the top rank, i.e., the highest SIF according to Eq. (1), among all other defects in the respective notched specimens.

Table 1 Information of all 17 fatigue critical defects observed in this study including their sizes measured via both XCT and fractography, normalized SIF, and absolute and relative ranking of critical defects in accordance with their SIF within the respective notched specimens as well as the details of the specimens. It should be noted that the critical defects' information is shown in the increasing order of critical defect sizes (i.e., 1st column) for both materials.

Size via XCT (μm)	Size via fractography (μm)	$K_{I(Max.)}/\sigma_{Max.}$	Abs. rank of critical defects	Relative rank of critical defects (%ile)	Specimen (Crack initiation site) ID	Material	Specimen geometry	ρ (mm)
28	19	6.0	1	99.320	1	17-4 PH SS	Cylindrical	50
45	24	5.9	1	99.457	2	17-4 PH SS	Cylindrical	50
54	50	25.4	1	99.978	3	17-4 PH SS	Flat	5
83	62	12.1	1	99.985	4	17-4 PH SS	Cylindrical	5
98	58	12.9	1	99.989	5	17-4 PH SS	Cylindrical	5
154	79	16.9	17	99.574	6	AlSi10Mg	Flat	5
162	113	14.0	15	99.423	7	AlSi10Mg	Cylindrical	50
179	114	15.6	18	99.377	8	AlSi10Mg	Cylindrical	5
200	149	16.3	1	99.976	9	AlSi10Mg	Flat	50
201	149	19.3	2	99.918	10	AlSi10Mg	Flat	5
222	181	17.5	1	99.973	11	AlSi10Mg	Flat	50
251	186	17.8	14	99.405	12	AlSi10Mg	Flat	50
257	141	21.8	1	99.965	13	AlSi10Mg	Flat	5
291	187	21.6	1	99.952	14 (Site 1)	AlSi10Mg	Cylindrical	5

346	244	25.4	1	99.952	14 (Site 2)	AlSi10Mg	Cylindrical	5
371	140	20.9	1	99.979	15 (Site 1)	AlSi10Mg	Cylindrical	50
377	194	20.7	1	99.979	15 (Site 2)	AlSi10Mg	Cylindrical	50

The SIF of the top rank defects, obtained utilizing the NDI-based approach and XCT data, were compared with the SIF of the experimentally observed fatigue critical defects from fractography, using Gumbel's largest extreme value statistics (LEVS). The SIF of the fatigue critical defects were calculated using Eq. (1) but with two different measures of size, namely via fractography and XCT. The obtained SIF were normalized using the maximum nominal stresses, i.e., making them independent of the applied nominal stress, during the fatigue testing for respective specimens, i.e., $K_{I(Max.)}/\sigma_{Max.}$. The reduced variate and the corresponding cumulative and probability density functions (CDF and PDF) for the normalized SIF of top rank defects according to the NDI-based approach and the actual fatigue critical defects are plotted in **Fig. 9**. The reduced variate measure, *V,* was calculated using:

$$V_i = -ln\,(-\,ln(i/\,N+1))\,, \tag{2}$$

where *i* and *N* are the rank and the total number of critical volumetric defects whose SIF were being analyzed [40]. The coefficient of determination, R^2, in all cases, was found to be higher than 0.8 (see **Fig. 9**(a)), indicating that the normalized SIF of top rank and fatigue critical defects followed a Gumbel distribution.

The CDF and PDF curves, shown in **Fig. 9**(b), show similarities between the normalized SIF of top rank and fatigue critical defects (defect sizes measured via both fractography and XCT). Such correlation between the top rank and the experimentally observed fatigue critical defects suggests the efficacy of the NDI-based approach to assess fatigue criticality of volumetric defects. Note, the distribution of the normalized SIF for the top rank defects (magenta curve in **Fig. 9**(b)) was much closer to the critical defects (blue curve in **Fig. 9**(b)) whose sizes were measured via XCT than to the critical defects measured via fractography (green curve in **Fig. 9**(b)). The normalized SIF of critical defects whose sizes were measured via fractography skewed towards smaller sizes. This is likely due to the overestimation of defect sizes by XCT. The methodology

implemented to post-process the XCT data to extract defects, shown in **Figs. 2**(a-d), including gradient operation followed by binarization (thresholding), likely resulted in an overestimation of the defect morphology detected via XCT.

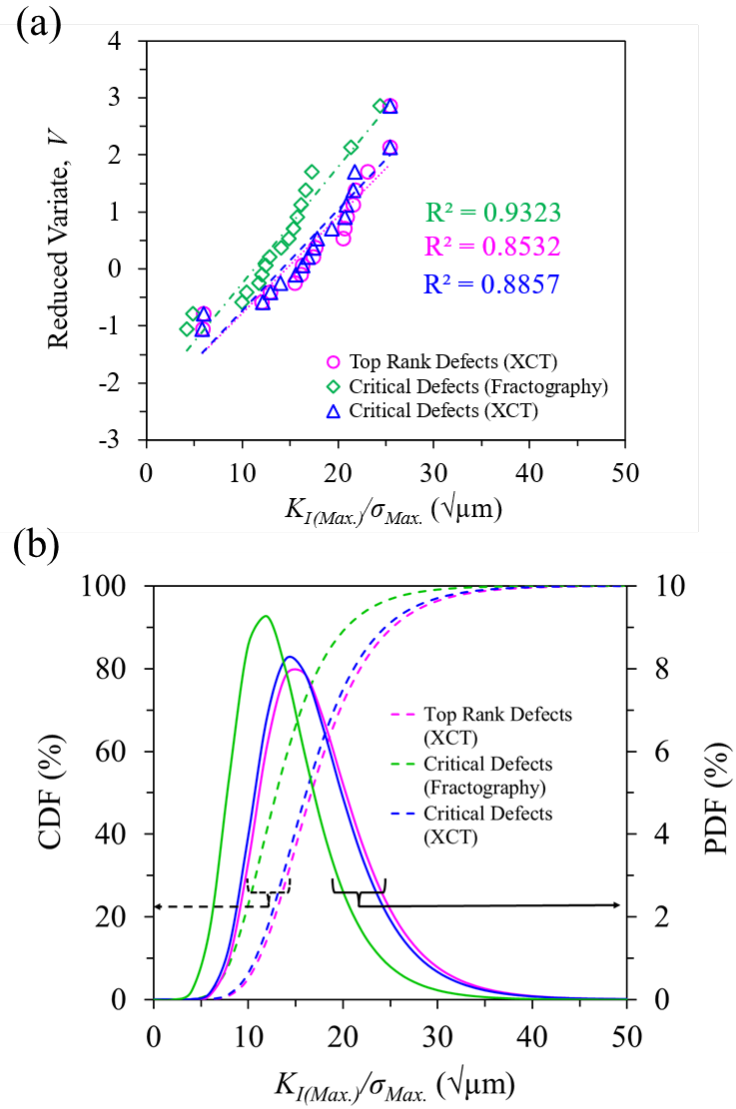

Fig. 9 (a) Reduced variate, (b) CDF, and PDF plots, according to LEVS [40], for normalized SIF of top rank defects obtained via the NDI-based approach, and the actual fatigue critical defects whose sizes were measured via fractography and XCT.

3.3 Limitations of the NDI-based approach

Out of the 17 fatigue critical defects (in 15 specimens) analyzed, 5 did not rank the highest SIF among the volumetric defects in their respective specimens. These unusual critical defects

were examined to understand the limitations of the approach. For these critical defects, XCT was unable to detect its true morphology, thus mischaracterizing their sizes and fatigue criticality. As examples, **Fig. 10** illustrates the use of the NDI-based approach in two such specimens. One such instance of XCT not being able to fully capture the critical defect's features occurred in the *ρ 5 mm* cylindrical AlSi10Mg specimen tested at 150 MPa. As shown in **Figs. 10**(a - c), XCT did not detect the fine intricate features of the critical LoF defect. This error caused the critical defect to be measured smaller than its true size which led to the mischaracterization of its fatigue criticality; the critical defect's SIF was lower than seventeen other volumetric defects within the notched specimen. Similarly, in **Figs. 10**(d - f), XCT could not detect the fine features of two nearby critical LoF defects. Despite these defects showing the highest SIF among other defects within the specimen, only partial morphologies were detected via XCT. Therefore, the resolution used during the XCT posed a limitation to the NDI-based approach to assess fatigue criticality of volumetric defects for these specimens.

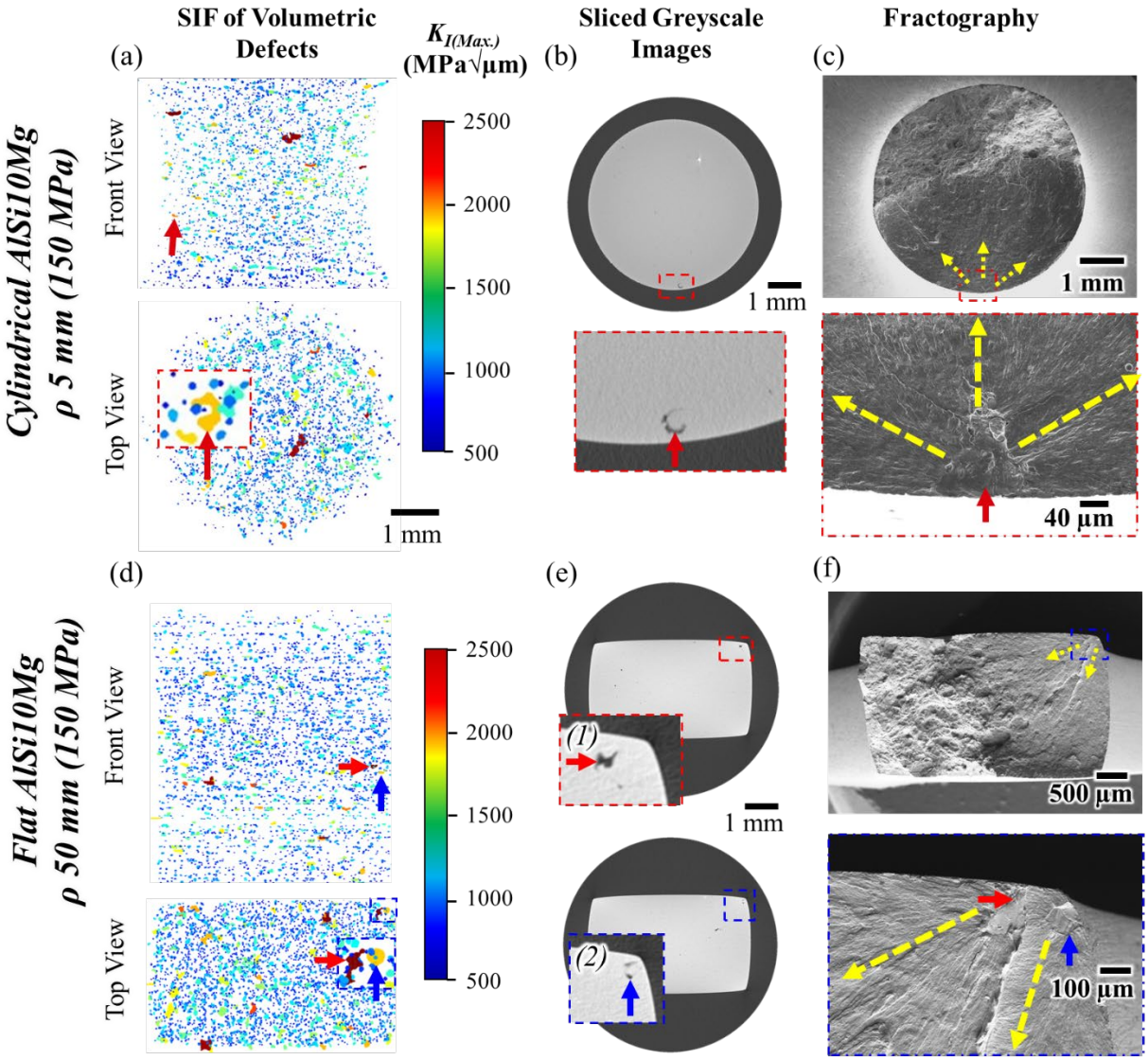

Fig. 10 (a, b) Visualization of volumetric defects, colored according to their SIF, within the XCT scan volume, (c, d) sliced greyscale XCT images showing the critical defects, and (e, f) fractography images showing the fatigue crack initiation sites in cylindrical and flat *ρ 5 mm* AlSi10Mg specimens.

Lastly, since the NDI-based approach was intended for techniques that can at least reveal the spatial and size information of volumetric defects, it cannot account for the fatigue crack initiation from only microstructural features (such as delta-ferrites (δ-Fe) in CA-H1025 17-4 PH SS). Out of 32 specimens that were analyzed and tested, 6 17-4 PH SS specimens showed fatigue crack initiation from δ-Fe precipitates. In the absence of large enough volumetric defects acting as

stress concentrators, these precipitates acted as weak points in the microstructure [41,42] and likely promoted fatigue crack initiation and growth along the δ-Fe-martensite interfaces to form crystallographic facets. As examples, the presence of crystallographic facets in the fatigue crack initiation sites for two 17-4 PH SS flat notched specimens from R batch with *ρ 5 mm* and *ρ 50 mm* is shown in **Fig. 11**.

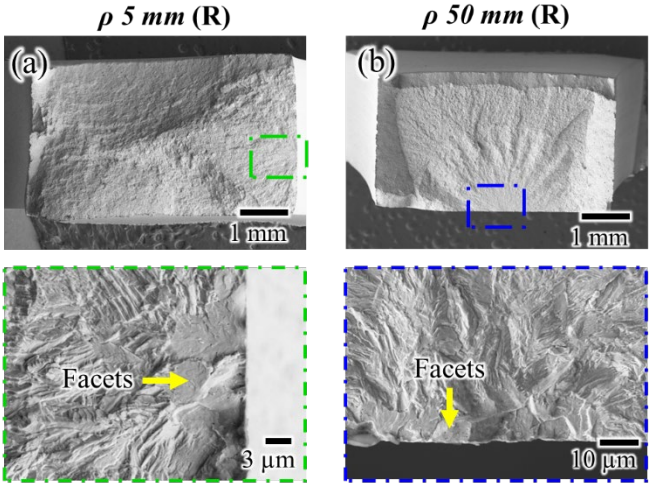

Fig. 11 Fractography images showing crystallographic facets in the fatigue crack initiation sites for (a) *ρ 5 mm* and (b) *ρ 50 mm* 17-4 PH SS flat notched specimens from R batch.

4 Conclusions

This study utilized linear elastic fracture mechanics to assess the fatigue criticality of volumetric defects in notched specimens detected via non-destructive inspection (NDI) techniques, specifically X-ray computed tomography. Assuming a defect-crack equivalency based on Murakami's approach, Mode-I stress intensity factor (SIF) of volumetric defects was calculated to represent their fatigue criticality. The linear elastic fracture mechanics approach, ($K_{I(Max.)} = Y\sigma_{Max.}K_{t(local)}\sqrt{\pi\sqrt{area}}$), accounted for defects' size and location as well as the local stresses due to the notch geometry, to calculate the SIF. Defects with higher SIF were considered as critical defects to initiate critical fatigue cracks. This behavior was validated using laser powder bed fused AlSi10Mg and 17-4 precipitation hardening stainless steel cylindrical and flat notched specimens with varying notch root radii (5 mm and 50 mm). All critical defects fell within the 99.3 percentile of the defects with the highest stress intensity factor in the respective specimen, demonstrating the

efficacy of the NDI-based approach. Despite the general success of the fatigue criticality assessment, some limitations were noted. These limitations included critical defects with features that were obscured by the resolution of the XCT and cases where defects did not contribute to critical crack formation.

Acknowledgments

This material is based upon work partially supported by the United States Army under Contract No. W56HZV-17-C-0095 and the National Science Foundation under Contract No. 2319690.

CRediT authorship contribution statement

Arun Poudel: Writing – original draft, Investigation, Methodology, Software, Visualization, Validation, Formal analysis, Data curation, Conceptualization. **Jonathan Pegues**: Writing – review & editing, Investigation, Methodology, Formal analysis, Data curation, Conceptualization. **Matthew Kelly**: Writing – review & editing, Resources, Methodology, Formal analysis, Conceptualization. **Shuai Shao**: Writing – review & editing, Methodology, Investigation, Formal analysis, Data curation, Conceptualization. **Nima Shamsaei:** Writing – review & editing, Supervision, Resources, Project administration, Methodology, Investigation, Funding acquisition, Formal analysis, Conceptualization.

References

[1] A. Yadollahi, N. Shamsaei, Additive manufacturing of fatigue resistant materials: Challenges and opportunities, Int J Fatigue 98 (2017) 14–31. https://doi.org/10.1016/J.IJFATIGUE.2017.01.001.

[2] J.C. Sobotka, M.P. Enright, R.C. McClung, Application of critical distances to fatigue at pores, Fatigue Fract Eng Mater Struct 42 (2019) 1646–1661. https://doi.org/10.1111/ffe.13004.

[3] S. Beretta, S. Romano, A comparison of fatigue strength sensitivity to defects for materials manufactured by AM or traditional processes, Int J Fatigue 94 (2017) 178–191. https://doi.org/10.1016/j.ijfatigue.2016.06.020.

[4] S. Afazov, A. Serjouei, G.J. Hickman, R. Mahal, D. Goy, I. Mitchell, Defect-based fatigue model for additive manufacturing, Progress in Additive Manufacturing (2022). https://doi.org/10.1007/s40964-022-00376-6.

[5] S. Shao, A. Poudel, N. Shamsaei, A linear elastic finite element approach to fatigue life estimation for defect laden materials, Eng Fract Mech 285 (2023) 109298. https://doi.org/10.1016/J.ENGFRACMECH.2023.109298.

[6] R. Molaei, A. Fatemi, N. Sanaei, J. Pegues, N. Shamsaei, S. Shao, P. Li, D.H. Warner, N. Phan, Fatigue of additive manufactured Ti-6Al-4V, Part II: The relationship between microstructure, material cyclic properties, and component performance, Int J Fatigue 132 (2020) 105363. https://doi.org/10.1016/j.ijfatigue.2019.105363.

[7] A. Fatemi, R. Molaei, J. Simsiriwong, N. Sanaei, J. Pegues, B. Torries, N. Phan, N. Shamsaei, Fatigue behaviour of additive manufactured materials: An overview of some recent experimental studies on Ti-6Al-4V considering various processing and loading direction effects, Fatigue Fract Eng Mater Struct 42 (2019) 991–1009. https://doi.org/10.1111/ffe.13000.

[8] A. Soltani-Tehrani, R. Shrestha, N. Phan, M. Seifi, N. Shamsaei, Establishing Specimen Property to Part Performance Relationships for Laser Beam Powder Bed Fusion Additive Manufacturing, Int J Fatigue (2021).

[9] N. Sanaei, A. Fatemi, N. Phan, Defect characteristics and analysis of their variability in metal L-PBF additive manufacturing, Mater Des 182 (2019) 108091. https://doi.org/10.1016/j.matdes.2019.108091.

[10] A. du Plessis, I. Yadroitsava, I. Yadroitsev, Effects of defects on mechanical properties in metal additive manufacturing: A review focusing on X-ray tomography insights, Mater Des 187 (2020) 108385. https://doi.org/10.1016/j.matdes.2019.108385.

[11] M. Seifi, M. Gorelik, J. Waller, N. Hrabe, N. Shamsaei, S. Daniewicz, J.J. Lewandowski, Progress Towards Metal Additive Manufacturing Standardization to Support Qualification and Certification, JOM 69 (2017) 439–455. https://doi.org/10.1007/s11837-017-2265-2.

[12] L. Levine, B. Lane, E. Glaessgen, M. Gorelik, Providing a Rigorous Benchmark Measurement Foundation for Modeling-Informed Qualification and Certification of Metal Additive Manufactured Components, JOM 76 (2024) 1897–1904. https://doi.org/10.1007/S11837-024-06388-7/FIGURES/2.

[13] W.E. Frazier, Metal additive manufacturing: A review, J Mater Eng Perform 23 (2014) 1917–1928. https://doi.org/10.1007/s11665-014-0958-z.

[14] B. Atzori, P. Lazzarin, Notch sensitivity and defect sensitivity under fatigue loading: Two sides of the same medal, Int J Fract 107 (2000) 1–10. https://doi.org/10.1023/A:1007686727207.

[15] K. Solberg, F. Berto, Notch-defect interaction in additively manufactured Inconel 718, Int J Fatigue 122 (2019) 35–45. https://doi.org/10.1016/j.ijfatigue.2018.12.021.

[16] J. Ferchow, D. Kälin, G. Englberger, M. Schlüssel, C. Klahn, M. Meboldt, Design and validation of integrated clamping interfaces for post-processing and robotic handling in additive manufacturing, International Journal of Advanced Manufacturing Technology 118 (2022) 3761–3787. https://doi.org/10.1007/S00170-021-08065-4/FIGURES/34.

[17] D. Arola, C.L. Williams, Estimating the fatigue stress concentration factor of machined surfaces, Int J Fatigue 24 (2002) 923–930. https://doi.org/10.1016/S0142-1123(02)00012-9.

[18] M. Åman, Y. Tanaka, Y. Murakami, H. Remes, G. Marquis, Fatigue strength evaluation of small defect at stress concentration, Procedia Structural Integrity 7 (2017) 351–358. https://doi.org/10.1016/J.PROSTR.2017.11.099.

[19] P. Livieri, R. Tovo, Fatigue limit evaluation of notches, small cracks and defects: an engineering approach, Fatigue Fract Eng Mater Struct 27 (2004) 1037–1049. https://doi.org/10.1111/J.1460-2695.2004.00816.X.

[20] B. Atzori, P. Lazzarin, G. Meneghetti, Fracture mechanics and notch sensitivity, Fatigue Fract Eng Mater Struct 26 (2003) 257–267. https://doi.org/10.1046/J.1460-2695.2003.00633.X.

[21] H. Villarraga-Gómez, C.M. Peitsch, A. Ramsey, S.T. Smith, The role of computed tomography in additive manufacturing, Proceedings - 2018 ASPE and Euspen Summer Topical Meeting: Advancing Precision in Additive Manufacturing (2018) 201–210.

[22] A. Du Plessis, I. Yadroitsev, I. Yadroitsava, S.G. Le Roux, X-Ray Microcomputed Tomography in Additive Manufacturing: A Review of the Current Technology and Applications, 3D Print Addit Manuf 5 (2018) 227–247. https://doi.org/10.1089/3DP.2018.0060/ASSET/IMAGES/LARGE/FIGURE13.JPEG.

[23] Z. Wu, Z. He, S. Wu, X. Gao, L. Lei, C. Liu, B. Chen, C. Dong, Rotating bending fatigue mechanisms of L-PBF manufactured Ti-6Al-4V alloys using in situ X-ray tomography, Int J Fatigue 176 (2023) 107876. https://doi.org/10.1016/J.IJFATIGUE.2023.107876.

[24] A. Tawfik, P. Bills, L. Blunt, R. Racasan, Development of an Additive Manufactured Artifact to Characterize Unfused Powder Using Computed Tomography, International Journal of Automation Technology 14 (2020) 439–446. https://doi.org/10.20965/IJAT.2020.P0439.

[25] X. Cai, A.A. Malcolm, B.S. Wong, Z. Fan, Measurement and characterization of porosity in aluminium selective laser melting parts using X-ray CT, Virtual Phys Prototyp 10 (2015) 195–206. https://doi.org/10.1080/17452759.2015.1112412.

[26] A. Du Plessis, S.G. Le Roux, G. Booysen, J. Els, Quality Control of a Laser Additive Manufactured Medical Implant by X-Ray Tomography, 3D Print Addit Manuf 3 (2016) 175–182. https://doi.org/10.1089/3DP.2016.0012/ASSET/IMAGES/LARGE/FIGURE8.JPEG.

[27] X. Gao, C. Tao, S. Wu, B. Chen, S. Wu, X-ray imaging of defect population and the effect on high cycle fatigue life of laser additive manufactured Ti6Al4V alloys, Int J Fatigue 162 (2022) 106979. https://doi.org/10.1016/J.IJFATIGUE.2022.106979.

[28] Y. Murakami, Metal Fatigue. Effects of Small Defects and Nonmetallic Inclusions, 2002.

[29] M.H. El Haddad, T.H. Topper, K.N. Smith, Prediction of non propagating cracks, Eng Fract Mech 11 (1979) 573–584. https://doi.org/10.1016/0013-7944(79)90081-X.

[30] M.D. Chapetti, Fracture mechanics models for short crack growth estimation and fatigue strength assessment, Matéria (Rio de Janeiro) 27 (2022). https://doi.org/10.1590/1517-7076-RMAT-2022-0030.

[31] M.H. El Haddad, K.N. Smith, and T. H Topper, E. Haddad, A. Strain, A Strain Based Intensity Factor Solution for Short Fatigue Cracks Initiating from Notches, 1979.

[32] D.B. Witkin, | D N Patel, | G E Bean, Notched fatigue testing of Inconel 718 prepared by selective laser melting, Fatigue Fract Eng Mater Struct 42 (2019) 166–177. https://doi.org/10.1111/FFE.12880.

[33] S. Afkhami, E. Dabiri, K. Lipiäinen, H. Piili, T. Björk, Effects of notch-load interactions on the mechanical performance of 3D printed tool steel 18Ni300, Addit Manuf 47 (2021) 102260. https://doi.org/10.1016/J.ADDMA.2021.102260.

[34] R.A. Smith, K.J. Miller, FATIGUE CRACKS AT NOTCHES, Pergamon Press, 1977.

[35] A. Poudel, J. Pegues, M. Kelly, S. Shao, N. Shamsaei, Fatigue Behavior of Additively Manufactured Cylindrical Notched Specimens: The Effect of Volumetric Defects, Eng Fail Anal (2025). https://doi.org/10.1016/j.engfailanal.2025.10960

[36] A. Poudel, J. Pegues, M. Kelly, S. Shao, N. Shamsaei, Fatigue behavior of additively manufactured edge notched specimens, Int J Mech Sci (2025). https://doi.org/10.1016/j.ijmecsci.2025.110315

[37] Y. Murakami, M. Endo, Effects of defects, inclusions and inhomogeneities on fatigue strength, Int J Fatigue 16 (1994) 163–182. https://doi.org/10.1016/0142-1123(94)90001-9.

[38] A.D.N.A. Committee, AMS2771: Heat Treatment of Aluminum Alloy Castings - SAE International, SAE International. https://doi.org/10.4271/AMS2771.

[39] Standard Specification for Precipitation-Hardening Stainless and Heat-Resisting Steel Plate, Sheet, and Strip.

[40] A. E2283-08, Standard Practice for Extreme Value Analysis of Nonmetallic Inclusions in Steel, 08 (2015) 1–11. https://doi.org/10.1520/E2283-08R19.1.

[41] R. Bussoloti, G.E. Totten, L.L.M. Albano, L.C.F. Canale, Delta Ferrite: Cracking of Steel Fasteners, in: Encyclopedia of Iron, Steel, and Their Alloys, CRC Press, 2016: pp. 1070–1081. https://doi.org/10.1081/e-eisa-120049491.

[42] T. Wegrzyn, Delta ferrite in stainless steel weld metals, Welding International 6 (1992) 690–694. https://doi.org/10.1080/09507119209548267.